HHS Public Access

Author manuscript

*Adv Mater Technol*. Author manuscript; available in PMC 2021 May 01.

Published in final edited form as:

*Adv Mater Technol*. 2020 May ; 5(5): . doi:10.1002/admt.201900960.

# Flow Homogenization Enables a Massively Parallel Fluidic Design for High-throughput and Multiplexed Cell Isolation

**Chinchun Ooi**[*],
Department of Chemical Engineering, Stanford University, Stanford, California, USA; Department of Fluid Dynamics, Institute of High Performance Computing, Singapore

**Christopher M. Earhart**,
Department of Materials Science and Engineering, Stanford University, Stanford, California, USA

**Casey E. Hughes**,
Division of Oncology, Department of Medicine, Stanford University School of Medicine, Stanford, California, USA; Department of Biochemistry, University of Utah School of Medicine, Salt Lake City, Utah, USA

**Jung-Rok Lee**,
Division of Mechanical and Biomechanical Engineering, Ewha Womans University, Seoul, South Korea

**Dawson J. Wong**,
Department of Electrical Engineering, Stanford University, Stanford, California, USA

**Robert J. Wilson**,
Department of Materials Science and Engineering, Stanford University, Stanford, California, USA

**Rajat Rohatgi**,
Department of Biochemistry, Stanford University School of Medicine, Stanford, California, USA

**Shan X. Wang**[*]
Department of Materials Science and Engineering, Stanford University, Stanford, California, USA; Department of Electrical Engineering, Stanford University, Stanford, California, USA

## Abstract

Microfluidic devices are widely used for applications such as cell isolation. Currently, the most common method to improve throughput for microfluidic devices involves fabrication of multiple, identical channels in parallel. However, this ‘numbering up’ only occurs in one dimension, thereby limiting gains in volumetric throughput. In contrast, macro-fluidic devices permit high volumetric flow-rates but lack the finer control of microfluidics. Here, we demonstrate how a micro-pore array design enables flow homogenization across a magnetic cell capture device, thus creating a massively parallel series of micro-scale flow channels with consistent fluidic and magnetic properties, regardless of spatial location. This design enables scaling in 2-dimensions, allowing flow-rates exceeding 100 mL/hr while maintaining >90% capture efficiencies of spiked lung cancer cells from blood in a simulated circulating tumor cell system. Additionally, this design

[*]Corresponding Author: ooichinchun@gmail.com, sxwang@stanford.edu.

facilitates modularity in operation, which we demonstrate by combining two different devices in tandem for multiplexed cell separation in a single pass with no additional cell losses from processing.

## Graphical Abstract

**Multiplexed and high-throughput cell separation** can be immensely useful in areas such as circulating tumor cell or circulating nucleated fetal cell isolation and analysis. This work details the physical principle behind a micro-pore design that utilizes a unique flow homogenization phenomenon to rapidly and simply separate a heterogeneous cell population into its subpopulations in a single pass with minimal processing losses.

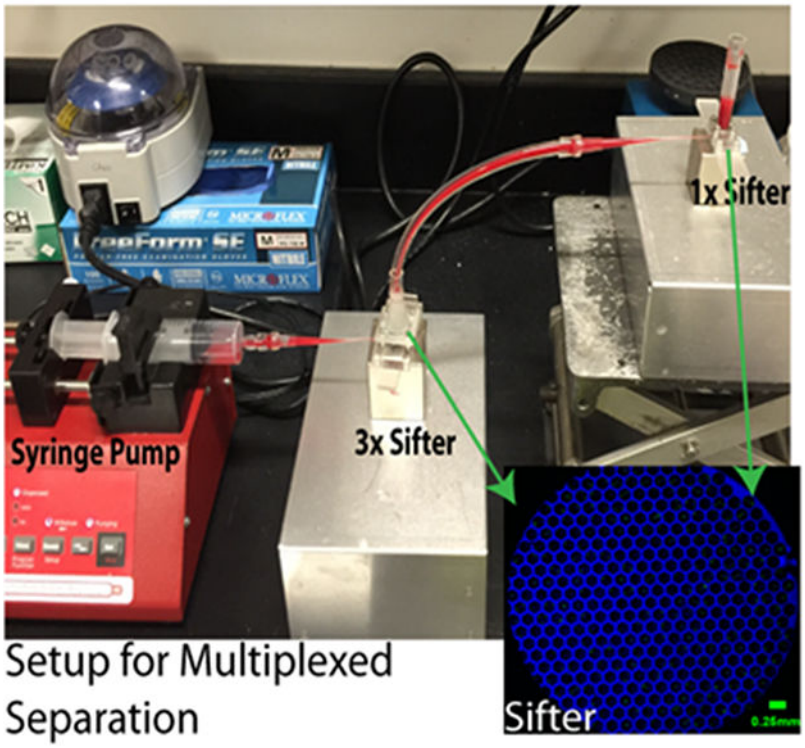


### Keywords

microfluidics; rare cell isolation; multiplexed cell separation; flow homogenization; magnetic separation

## 1. Introduction

Microfluidics has been immensely impactful over the past decade, as researchers have found new ways to apply the unique physics and characteristics of that regime to myriad applications such as single cell sequencing,[1–3] green chemistry,[4, 5] and cell isolation and manipulation.[6–10] While the reduced processing volume is beneficial for many applications such as point-of-care diagnostics,[11, 12] high volumetric flow rates are necessary for increased throughput in other instances. A pertinent example is in rare cell isolation,[13] such

as the isolation and analysis of circulating tumor cells (CTCs), where 7.5 mL of blood is typically processed per patient,[14, 15] or circulating fetal nucleated cells, with rarity of < 6 cells per mL of maternal blood.[16] Although there have been some ingenious designs that can still achieve relatively high flow-rates, especially in the field of CTC isolation,[17–22] in general, microfluidics can be disadvantageous due to difficulties in scaling. Indeed, increasing through-put in many microfluidic devices is typically accomplished by 'numbering up', i.e. increasing the number of parallel channels,[23, 24] to ensure operation within the same characteristic length scales and optimal performance. However, 'numbering up' requires potentially complex control over flow distributions, and is not always straightforward with regards to fabrication.[4]

On the other end of the scale, flow-through macro-fluidic devices are frequently used to accomplish goals such as cell isolation.[25–29] These devices can be effective and frequently have much higher through-put, but they typically do not present the user with as much fine-grained control as microfluidic devices. Consequently, challenges remain in optimizing for performance. As device designs that can combine the high volumetric throughput typical of macro-fluidic designs with the micro-scale control of micro-fluidic designs are relatively rare or complex, microfluidic and macro-fluidic devices are typically viewed as two complementary designs, with their respective advantages and disadvantages.

Our group previously published a macro-fluidic design for magnetic cell or nanoparticle separation, with high capture efficiencies at fast volumetric flow rates, but with little discussion regarding the impact of inhomogeneities across the entire device on scalability.[30] In the following sections, we first demonstrate how the magnetic sifter can scale in area (and volumetric flow rate) with no drop-off in capture efficiency when applied to the isolation of simulated rare circulating tumor cells from blood, without any additional engineering or optimization. We then used finite element simulations and further experimental validation to explain how this scaling results from a flow homogenization phenomenon. We show how the magnetic sifter's micro-pore structure acts analogously to flow-through screens that shape the flow field profile for wind and water tunnel experiments in applications such as marine engineering or aeronautical engineering,[31–34] and illustrate how the device causes flow homogenization due to the high fluidic resistance through each micro-pore. Consequently, each micro-pore in the magnetic sifter acts as an independent 'virtual micro-fluidic channel', thus facilitating massive scaling-up of the device in a manner akin to the parallelization commonly used in 'numbering up' microfluidic devices, but on a macro-fluidic scale. It is important to note here that these channels are 'virtual' in the sense that it is unlike the typical 'numbering up' of microfluidic devices where actual individual microfluidic channels are fabricated on the chip, but the flow naturally splits across all the micro-pores due to the high fluidic resistance with no fabrication of explicit physical fluid channels.

More pertinently, flow focusing in microfluidics has long been utilized as a primary means of control for various applications such as cell counting and analysis.[35–39] The flow homogenization phenomenon presented here can similarly be applied towards the scaling of these devices to achieve high performance and throughput simultaneously. For example, the typical application of cell counting can be accomplished by directly fabricating electrodes

on the boundaries of each micro-pore to count the number of cells traversing each micro-pore.

Lastly, the planar nature of this micro-pore array also facilitates flexible combinations of devices for different functionality and modular design, akin to how one can put different designs such as an inertial focusing section and a magnetic separation section in sequence in a single microfluidic device.[17, 40] Hence, we demonstrate here a proof-of-concept with results for a tandem setup comprising two different versions of our magnetic sifter to effect multiplexed cell separation in a single pass, with no additional cell losses.

## 2. Results

### 2.1. Magnetic Sifter Operating Principle

The magnetic sifter is a micro-pore array coated with a soft magnetic material with good capture performance in the isolation and release of magnetically-labeled circulating tumor cells in non-small cell lung cancer (NSCLC).[30, 41] The device consists of a 12 μm thick permalloy ($Ni_{81}Fe_{19}$) film with a regular tessellation of 40 x 40 $\mu m^2$ pores etched through it, supported on a honeycomb silicon skeleton, as illustrated in Figure 1.[42] When magnetically labeled entities such as cells in blood are flowed through the sifter with a magnetic field applied, the thin magnetic film is magnetized and generates magnetic forces within the pores that capture the magnetic entities against the flow. Upon removal of the external magnetic field, the soft magnetic field is no longer magnetized, and the magnetic entities can then be eluted from the device. The honeycomb silicon skeleton was selected due to prior literature suggesting such designs retain good mechanical strength while permitting a large degree of porosity, which is desirable for higher volumetric flow-rates.[43] An arrangement of 7 40 × 40 $\mu m^2$ pores was selected for each array in conjunction with prior finite element simulations showing that such an arrangement can maximize the magnetic field gradient within each pore, and consequently, capture efficiency.[42]

### 2.2. Simulated CTC Capture Efficiencies with Scaled-up Magnetic Sifters

Three differently-sized sifters were then designed and fabricated to investigate the capability for scaling the magnetic sifter's volumetric throughput in a 2-dimensional manner. The 3 sets of sifters were fabricated in the same fabrication run to minimize any batch-to-batch variability, and were tested with the same batch of cells and reagents. These three differently-sized sifters have actual active areas (region in contact with the fluid sample) of 5 × 5 $mm^2$, 10 × 10 $mm^2$ and 15 × 15 $mm^2$, and are referred to in subsequent sections as the '1X Sifter', the '2X Sifter' and the '3X Sifter' respectively, with reference to their increasing size and linear scaling. Critically, for each device size, the actual micro-pore dimension as depicted in Figure 1(d) is maintained at 40 × 40 $\mu m^2$, although the total number of micro-pores per device (N) scales with the linear dimension of the sifter active area (L) as $N \propto L^2$.

We then tested the performance of these sifters by evaluating their capture of NCI-H1650 cells (a NSCLC cell line) that had been spiked in healthy donor blood to simulate a circulating tumor cell sample. These cells were labeled with magnetic nanoparticles via the Epithelial Cell Adhesion Molecule (EpCAM) surface antigen, and magnetically isolated

with the magnetic sifter across a range of flow rates. The proportion of spiked H1650 cells successfully isolated (capture efficiency) are presented in Figure 2 and show a similar dependence on flow rate across sifters of all 3 sizes. Critically, when their capture efficiencies are plotted against linear flow velocity through the respective magnetic sifters as in Figure 2(b), the capture efficiencies for all 3 sets of differently-sized sifters overlap, indicating how the sifter's capture performance scales reproducibly and linearly with the surface area of the chip.

### 2.3. Experimental and Numerical Verification of Flow Homogenization across the Magnetic Sifter

Finite element simulations of the hydrodynamic profile across the magnetic sifter were then conducted with Comsol Multiphysics software to better understand the scaling observed in Figure 2. The results in Figure 3(a) illustrate how the flow field is homogenized across the sifter, as the typical parabolic velocity profile that develops due to the no-slip boundary condition of the inlet tubing's sidewalls transitions to a relatively homogeneous flow field near the entrance to the sifter.

Critically, as depicted in Figure 3(b), this homogenization results in flow fields across 96% of the sifter pores having velocities within 10% of the mean velocity across all pores in the sifter, hence suggesting there is minimal variance in each micro-pore's fluid velocity regardless of the micro-pore's spatial location across the sifter, There are outliers in Figure 3(b) with relative linear velocities of 1.3×, but they correspond to the flow through the centermost pores, and comprise just 1.5% of all pores on the sifter.

This flow homogenization was further empirically verified by flowing fluorescently-labeled NCI-H1650 cells through the magnetic sifter after labeling with magnetic nanoparticles, and observing the capture location of these cells on the sifter, as depicted in Figure 4. This was done with fluid volumes containing 100 cells, 500 cells, and 1000 cells, with similar results across the range of cells tested. Saturation effects are expected at higher cell numbers whereby the capture of one cell might impact the capture location of subsequent cells. However, lower cell numbers are used here to deliberately avoid such saturation effects so as to better illustrate the flow, and the similar results across the range tested here further support the lack of saturation here.

Kolmogorov-Smirnov tests (KS-tests) are a non-parametric statistical test commonly used to compare samples with a reference probability distribution, and were used here to compare the experimentally observed spatial distribution of cells on the sifter with predicted cumulative probability distributions.[44, 45] When testing the null hypothesis that the experimental distribution is identical to the predicted distribution resulting from a parabolic flow profile, which is typical of laminar flow through a channel, the KS-test yielded a p-value $< 0.05$, indicating the experimental distribution is statistically very distinct from that expected for a parabolic flow.

However, when compared to the distribution expected for cells in a uniform, homogeneous flow field, the KS-test yielded a p-value of 0.29, which suggests the experimental results are not significantly different from the predicted distribution if the cells have approximately

uniform probability of being caught across any pore on the chip, regardless of the pore's actual location. Physically, this suggests that the similar flow velocities through each pore causes the cells to have equal probability of flowing through and being caught in any individual pore, regardless of spatial location across the sifter.

Having observed this phenomenon experimentally, we then sought to understand and explain this by measuring and analyzing the driving pressures required for fluid flow through the magnetic sifter both through experimental measurements, and numerical simulations via Comsol as per the schematic in Figure 5(a) and Figure 5(b). Using a digital manometer, we recorded the driving pressures across the sifter at different flow rates via the setup depicted in Figure 5(c), and compared the values to numerical simulations of the sifter.

There is relatively good correspondence between the predicted pressures from numerical simulations, and our experimentally measured results, as presented in Figure 5(f), although there appears to be increasing disparity at higher flow velocities. This could be due to the fluid flow at faster velocities approaching the limits of the fully laminar regime ($Re < 1$), while our numerical simulation models did not consider turbulence. Nonetheless, even at the highest velocity measured, the experiments and simulations differ by only 29%. The agreement between simulation and experiment further confirms the validity of the simulation results, and provides evidence for the existence of this flow homogenization.

### 2.4. Theoretical Analysis of Flow Homogenization and Magnetic Capture across the Magnetic Sifter

We then compared the simulated results and experimental measurements with a simplified theoretical model developed by Dagan et al. which treats the flow simply as a combination of Sampson flow before the pores and Poiseuille flow within the pores.[46] Notably, discrepancies are expected as this theoretical model was derived for an axisymmetric cylindrical pore, and not a square micro-pore as fabricated in this work. Additionally, the sifter actually has more occluded area than a regularly repeating micro-pore array as assumed in this theoretical model. In the actual sifter, the micro-pore array is mechanically supported on the honeycomb silicon skeleton, which surrounds every group of 7 micro-pores, as is obvious from the inset of Figure 1(c) and Figure 4(a). This is accounted for in the numerical simulations, as the geometry is explicitly modeled, but not the theoretical model, which assumes a fully periodic array of the micro-pores. This is expected to increase the actual fluidic resistance as these solid regions further increase obstruction to flow. Nonetheless, despite the expected discrepancy, we use this theoretical model by Dagan et al. to explain the large fluidic resistance caused by the micro-pore structure.

According to this simplified theoretical model by Dagan et al.[46], the driving pressure required for fluid flow through the micro-pore array is closely approximated by:

$$\Delta P = \frac{\mu Q}{\left(\frac{d}{2}\right)^3}\left(\frac{16}{\pi}\frac{t}{d} + 3\right) \quad (1)$$

where Q is the volumetric flow rate through each pore, d is the hydrodynamic diameter of the pore, t is the thickness of the pore and μ is the fluid viscosity, with a simple dependence

on the aspect ratio of the pore. Using our specific setup dimensions, where Q ≈ $10^{-12}$ $m^3$ $s^{-1}$ per pore, d = 40 μm (length of one side of each square pore), t = 12 μm and μ = $10^{-3}$ Pa·s, we obtain a pressure drop of 0.57 Pa across each pore in the sifter from Equation (1).

On the other hand, we can also estimate the pressure drop through a section of tubing, alternatively labeled as 'Fluid Connectors' in Figure 5(c), via the Darcy-Weisbach equation:

$$\Delta P = 32\mu L\frac{v}{D^2} \quad (2)$$

where μ is the fluid viscosity, L is the length of the channel, v is the average fluid velocity through the channel, and D is the hydrodynamic diameter of the channel. Assuming values typical of our setup where L = 500 μm, D = 5 mm and v = 0.15 mm $s^{-1}$, the pressure drop across a 500 μm length of tubing with the same cross-sectional area as the magnetic sifter would be 3 x $10^{-6}$ Pa from Equation 2.

This 5-order of magnitude difference in pressure is indicative of the greatly increased fluidic resistance caused by the micro-pores relative to the connective tubing, and provides intuition for the homogenization that occurs across the entire device. Essentially, the increased resistance to flow across each micro-pore far exceeds any additional resistance experienced due to resistance from the tubing surfaces, hence removing any dependence on spatial location on the sifter, and ensuring very similar flow across all pores.

While the assumptions behind the derivation of Equation 1 are not a perfect match for our current micro-pore array design, Equation 1 is important as it allows us to estimate the range of geometries over which this flow homogenization phenomenon will be valid. As the hydrodynamic diameter of the micro-pore increases, the effect of the Sampson flow component of Equation 1 is no longer significant relative to the Poiseuille flow component, and an inverse-cubic dependence of pressure on diameter (d) results. For our typical conditions above, a 40x increase in hydrodynamic diameter from 40 μm to 1.8 mm would reduce the resistance across each micro-pore sufficiently to remove any potential flow homogenization.

Taken together, our experimental and simulation results demonstrate how the micro-pore array design utilized in the magnetic sifter homogenizes flow through the chip, while the pressure analysis provides physical intuition for how this develops and a design guideline for predicting the occurrence of this phenomenon in similar micro-pore arrays with different pore length scales.

This flow homogenization causes the flow profile through each micro-pore to be spatially independent and identical, thus allowing the sifter to be scaled in both planar dimensions with a predictably consistent effect on overall device performance. In the instance of the magnetic sifter, this consistent scaling of the capture performance can be further understood qualitatively by analyzing the force balance between magnetic and fluidic forces acting on each cell as it traverses a single pore in the magnetic sifter. Briefly, the magnetic force acting on each magnetically-labeled cell is:

$$F_{mag} = (\vec{m} \cdot \nabla)\vec{B} \tag{3a}$$

$$F_{mag,\,sat} = m_s \left( \frac{\vec{B}}{|\vec{B}|} \cdot \nabla \right) \vec{B} \tag{3b}$$

where B is the magnetic field vector, m is the magnetic moment of the magnetically-labeled cell, and $m_s$ is the saturation magnetization of the magnetically-labeled cell, while the hydrodynamic force acting on each magnetically-labeled cell, assuming Stokes flow, is:

$$F_{drag} = 6\pi r \mu V_{cell} \tag{4}$$

where r is the cell's radius, μ is the fluid viscosity and $V_{cell}$ is the velocity of the fluid relative to the cell.

Based on previous Maxwell finite element simulations, the average magnetic field gradient is estimated at approximately $10^3$ T $m^{-1}$, while the magnetically labeled cells are estimated to have saturation magnetization of approximately $1.25 \times 10^{-13}$ A $m^2$ per cell.[30, 42] From Equation 3b, the magnetic force is thus estimated to be on the order of $1.25 \times 10^{-10}$ N. Similarly, using typical viscosity of water of $10^{-3}$ Pa·s, cell diameter of 15 μm, and linear velocities of $10^{-4}$ m $s^{-1}$, Equation 4 provides an estimate for hydrodynamic forces of approximately $1.4 \times 10^{-11}$ N for volumetric flow rates of approximately 10 mL $hr^{-1}$ on the 1X sifter.

For the magnetically labeled cell to be captured at any particular sifter pore, the magnetic force (Equation 3b) exerted due to the magnetic sifter must overcome the hydrodynamic drag forces (Equation 4) pushing the cell through the pore. The order of magnitude difference between estimated hydrodynamic and magnetic forces thus explains the relatively high capture efficiencies when the 1X sifter is operating at 10 mL $hr^{-1}$. Additionally, when the flow velocity through the pores are identical regardless of spatial location, the hydrodynamic drag forces are also identical, since the rest of the terms in Equation 4 are constant, and the corresponding magnetic force required per cell will be identical. Hence, flow homogenization across the sifter ensures that the capture performance for each pore in the array is consistent even when the sifter is scaled up.

### 2.5. Improved Capture Efficiencies at the Same Volumetric Throughput with Larger Magnetic Sifters

As with any antigen-based cell selection method, capture performance can vary with the expression level of the antigen. With reference to Equation 3(b), one can see that when antigen expression is low and the extent of magnetic labeling (magnitude of $m_s$) is consequently lowered, there will be a decrease in magnetic force. This will then lead to a decrease in capture performance for the same flow rate across the sifter, and correspondingly identical magnitude of hydrodynamic drag force.

A compromise solution is to decrease the magnetic sifter's operating volumetric flow rate to ensure effective capture of cells with a lower magnetic moment, but this will lead to an increase in processing time for the same sample volume. However, this decrease in volumetric flow-rate can be circumvented by increasing the size of the magnetic sifter, as the decrease in linear velocity can be avoided simply by increasing the number of pores on the sifter.

We thus proceeded to test this principle by evaluating the capture efficiency of Panc-1, a pancreatic cancer cell line that has been previously reported to have low EpCAM expression levels.[30] Measurements by flow cytometry showed that our H1650 cell line had an EpCAM expression level of $2.1 \pm 0.2 \times 10^5$ EpCAMs / cell, while the Panc-1 cell line had average EpCAM expression levels of $9.9 \pm 0.4 \times 10^3$ EpCAMs / cell, as per Figure 6(a). Having over an order of magnitude lower EpCAM expression level, the Panc-1 cell line exhibited markedly lower capture efficiencies on the 1X Sifter, with a mean capture efficiency of 19% at 10 mL $hr^{-1}$. However, by using the 15 x 15 $mm^2$ 3X sifters, the Panc-1 cells were isolated with 91 % capture efficiency at the same volumetric flow rate of 10 mL $hr^{-1}$, as shown in Figure 6(b).

## 2.6. Tandem Setup for Multiplex Enrichment by Antigen Expression Levels

In addition to the improvement in capture performance possible with this design, the planar flow-through nature of this design also facilitates modular addition of components to the entire flow system. We thus designed and constructed a tandem setup comprising a 1X sifter and a 3X sifter in series to simultaneously isolate and segregate circulating tumor cells by their relative EpCAM expression levels. In this tandem setup, the output from a $5 \times 5$ $mm^2$ active area (1X) magnetic sifter is directly fed into a $15 \times 15$ $mm^2$ active area (3X) sifter by connective tubing, while operating under the same volumetric flow rate in a continuous flow-through system, as illustrated in Figure 7(a).

Two cell lines (NCI-H1650 and Panc-1) with differing levels of EpCAM expression were spiked into blood at similar, physiologically relevant cell concentrations (~ 100 cells $mL^{-1}$ of blood), and processed through the magnetic sifters at 10 mL $hr^{-1}$. After magnetic labeling, the H1650 cells with very high levels of EpCAM expression have a higher level of magnetic loading and can be captured at faster flow rates, while the Panc-1 cells can only be captured at lower flow rates. By utilizing their differential ability to be captured at the same flow rates, we demonstrate a straightforward duplex separation of a simulated heterogeneous circulating tumor cell population with 2 distinct levels of EpCAM expression, as illustrated in Figure 7(b).

In the proof-of-concept experiments presented, we show how a single run through the tandem setup can separate a heterogeneous cell population into a subpopulation that is enriched for high EpCAM expression cells (H1650 cells) to an average of 83 % of total cells from the 1X sifter, and a different subpopulation that is enriched for low EpCAM expression cells (Panc-1 cells) to an average of 93 % from the 3X sifter. Critically, the total capture efficiency for both cell lines remained high, with a mean of 93 % for H1650 cells, and 89 % for Panc-1 cells, with the heterogeneous population being separated into its subcomponents without any further processing required, and with minimal additional cell losses.

## 3. Discussion

In this work, we have demonstrated how a micro-pore design for fluidic systems permits high volumetric flow rates while retaining single-cell interrogation of cell suspensions. In this work, the results shown are for direct rare cell isolation from whole blood, with associated cell concentrations of $10^9$ cells $mL^{-1}$ of blood. This is comparable to other isolation methods which do not require pre-processing of whole blood, and is simpler than other methods such as flow cytometry where red blood cell lysis or dilution with cell media might be required to reduce the actual cell density during operation. Importantly, our results are consistent with prior experiments in much more dilute cell suspensions of $10^5$ to $10^6$ cells $mL^{-1}$, with no degradation in capture efficiencies at similar flow-rates.[42] This indicates the sifter's ability to handle ≈ 50 % cell volume cell suspensions (whole blood) without compromising capture efficiencies, and consequently, the ability to process a wide range of realistic cell concentrations (from $10^5$ cells / mL to $10^9$ cells / mL). While we have chosen to minimize the current device's physical footprint to range from 5 × 5 $mm^2$ active areas to 15 × 15 $mm^2$ active areas, the flow homogenization phenomenon implies that the device can be easily scaled up in area through standard lithographic and microfabrication techniques. A simple 3× linear scaling of the device already allows volumetric flow rates to be adjusted above 100 mL $hr^{-1}$ while retaining a small device footprint (< 2 cm) and maintaining high capture efficiency (> 90 %) for simulated circulating tumor cells.

Nonetheless, due to the operating principle of the magnetic sifter being the capture of cells at the pores, saturation effects will occur when a large number of cells of interest are present, and the pores fill with capture cells. Our experiments indicate that this will occur when approximately $10^4$ cells have been captured on the 1X sifter, which corresponds to approximately 4 – 5 captured cells per pore. The described phenomenon in this work however suggests that the performance can scale simply with the active area, which suggests that a viable way to capture > $10^4$ cells of interest from a single pass is to use a 3X or 4X sifter.

Critically, magnetic separation was done with only a single pass through the sifter at very high volumetric flow rates, thus simplifying sample handling and reducing processing time. When handling rare cells like circulating tumor cells, this could be of great importance in ensuring high viability CTC recovery for effective downstream analysis. It is also important to note that other devices have been reported in literature with a similar operating principle, with a similar ability to capture magnetically labeled pathogens and cells at high flow-rates, and it is expected that the flow homogenization described here will explain their ability to scale similarly well. [47, 48]

Another unexpected benefit of this approach to scaling up volumetric flow rates is the avoidance of high fluidic pressures and consequently, any issues with mechanical reliability. In operation, even at relatively higher volumetric flow rates, the difference in pressure across the sifter's pores is only on the order of 10 Pa, and we have not experimentally observed any mechanical failure in the sifter even when operating at flow rates on the order of $10^2$ mL $hr^{-1}$. Qualitatively, this can be explained by the enhanced mechanical strength and flexural stiffness reported for such honeycomb skeleton designs, and the relatively thick permalloy

membranes used.[43] Permalloy has been reported to have a yield stress of approximately $10^8$ Pa, a Young's modulus of approximately $1 – 2 \times 10^{11}$ Pa, and a Poisson's ratio of approximately 0.25 – 0.30.[49,50] A maximum stress on the order of $10^3$ Pa and a peak displacement on the order of $10^{-13}$ m can be estimated using basic plate theory,[51,52] which is 5 orders of magnitude smaller than the typical yield stress of permalloy and 8 orders of magnitude smaller than the thickness of the membrane ($10^{-5}$ m) respectively, further explaining the lack of any significant issues with mechanical reliability.

Surprisingly, while prior work exists suggesting that certain cell marginalization can occur during flow, [53, 54] which might cause the capture of cells to be confined to certain regions within the micro-chip even with this flow homogenization effect, we did not observe such a bias in our work. This could be due to the simulated sample having been mixed prior to loading onto the chip and the high volumetric flow rates causing the complete passage of the sample through the device before the marginalization can occur.

Additionally, we demonstrated how this system can be extended to effect multiplex separations of the circulating tumor cell population into distinct subpopulations by antigen expression level. As a proof-of-concept, a tandem system with 2 sifter sizes was shown to separate a simulated heterogeneous population back into their constituent subpopulations in a single pass. Fabrication of other sifter sizes could conceivably allow one-step separation of a heterogeneous circulating tumor cell population into finer subpopulations based on antigen expression in a manner akin to what is typically done with flow cytometry, but with potentially less setup and processing time. Naturally, the resolution of this separation is still dependent on the degree to which the cell population of interest is multimodal in expression level. However, as our understanding of CTCs improve, including the role of biological pathways such as epithelial to mesenchymal transition (EMT), this approach may prove useful in further segregating CTCs by phenotype, and profiling of a patient's tumor.[55–57]

The separation efficiencies and purities here of approximately 90 % and 80 – 90 % are similar to other devices focusing on nanoparticle-mediated binning and profiling of heterogeneous cell populations. For example, in work by Reza et al.,[58] they showed that in experiments with cell lines with a 10-fold difference in EpCAM expression level, which is similar to the relative expression level between the H1650 and Panc-1 cell lines, approximately 80 % of Vcap cells (the higher EpCAM-expressing cell line) and 20 % of SKBR3 cells (the lower EpCAM-expressing cell line) were captured in their first zone and approximately 50 % of SKBR3 cells and 10 % of Vcap cells were captured in their second zone. This further suggests that such an approach may be of similar benefit in analyzing and separating heterogeneous cell populations, as was done in their work. Nonetheless, it is worth acknowledging that other processing methods might still be necessary down-stream of this device for purposes such as single-cell sequencing, where extremely high purities are necessary. However, it is anticipated that this pre-enrichment would already help reduce the amount of processing time required for methods such as flow cytometry.

While the tandem system was used here to connect two differently-sized sifters, the modularity of this system suggests easy sequential stacking of devices with different functionalities. The flow homogenization principle also lends itself to adaptation of various

microfluidic devices to facilitate scaling up to faster volumetric flow-rates, and/or possible integration with such a system for increased multiplexing of functionality. For example, the conventional MEMS processing used for fabrication of these flow devices lends itself to the integration of optical or electrical measurements at each micro-pore, and subsequent counting or sizing of particles and cells passaging through the micro-pores for purposes such as immunoassays which have typically also been done with microfluidics or other methods.[59–61]

## 4. Conclusion

In this work, we demonstrated the use of a regular microporous structure for flow homogenization, and the harnessing of this for devices that both exhibit high volumetric throughput and micro-scale control akin to that present in typical microfluidic channels. In this particular example, we isolated rare cells from healthy donor blood in a simulated circulating tumor cell system, in a similar manner to typical microfluidic magnetic capture, but on a massively parallel scale. However, this design should be easily adaptable to other microfluidic devices previously published, such as Coulter counters, for greatly improved volumetric throughput, while maintaining similar performance through each ‘virtual micro-channel’.

We also demonstrated the modular nature of this device with our tandem setup, suggesting how differently designed devices can be combined for increased functionality in a single pass. The planar nature of this design further facilitates combination of devices in series while minimizing the eventual system’s total physical footprint, and could simplify the development of other integrated microfluidic-like devices for various biomedical purposes.

## 5. Experimental Section

### Fabrication and Setup of the Magnetic Sifter and Holder:

Fabrication of the magnetic sifter has been previously described by Earhart et al.[30] Samples are currently loaded on the device by manual pipetting and pulled through the sifter by a syringe pump (New Era Pump Systems Inc., Model Number NE-1000). Neodymium-iron-boron (NdFeB) magnets purchased from K&J Magnetics, Inc. (Pipersville, PA) are used to magnetize the sifter. The magnetic sifter chips were fabricated with assistance from University of Michigan’s Lurie Nanofabrication Facility, and subsequently sputtered with the soft magnetic material, permalloy ($Ni_{81}Fe_{19}$), and a thin passivation layer of silicon dioxide via a Perkin Elmer high-vacuum RF-sputtering system. The $5 \times 5$ mm$^2$, $10 \times 10$ mm$^2$ and $15 \times 15$ mm$^2$ sifters were all designed on the same photolithography mask, and were fabricated in the same processing run. The individual sifter holders were custom-made by laser-cutting acrylic pieces in the Stanford Product Realization Lab and 3D-printing tube connectors in the Stanford 3-Dimensional Printing and Rapid Prototyping Facility.

### Cell Culture:

Both NCI-H1650 and Panc-1 cell lines were purchased from ATCC (Manassas, VA, USA). All cell lines were passaged in RPMI-1640 media (Thermo Fisher Scientific, Waltham, MA, Catalog number: 21870-076) with the following additives: 10% fetal bovine serum (FBS)

(Thermo Fisher Scientific, Waltham, MA, Catalog number: 10082-147), 0.05 mg/mL penicillin and streptomycin (Thermo Fisher Scientific, Waltham, MA, Catalog number: 15140-122), 2 mM GlutaMAX (Thermo Fisher Scientific, Waltham, MA, Catalog number: 35050-061), 1 mM sodium pyruvate (Thermo Fisher Scientific, Waltham, MA, Catalog number: 11360-070) and 0.1 mM MEM non-essential amino acid supplement (Thermo Fisher Scientific, Waltham, MA, Catalog number: 11140-050). The cell lines were maintained in an incubator at 37 $^{o}$C in 5 % $CO_2$.

### Simulated Circulating Tumor Cell Experiments:

Cultured cells were stained with either Green CellTracker CMFDA dye or Red CellTracker CMTPX dye (Invitrogen, Carlsbad, CA, Catalog number: C7025 and C34552) as per the dyes' provided protocols. They were then trypsinized and added to 2 mL of healthy donor blood from Stanford Blood Center in a microcentrifuge tube. The donor blood was always obtained day of the experiment from the Stanford Blood center in an EDTA tube. The number of spiked cells was counted under a fluorescence microscope before being added to the blood, and ranged between 100 and 300 cells per experiment. The spiked blood sample was then mixed with an equal volume of phosphate-buffered saline (PBS) media (Thermo Fisher Scientific, Waltham, MA, Catalog number: 10010-023) supplemented with 0.5 % bovine serum albumin (Sigma-Aldrich, St Louis, MO, Catalog number: B4287), 2 mM EDTA (Thermo Fisher Scientific, Waltham, MA, Catalog number: 15575-020) and 0.2% Pluronic F-68 solution (Thermo Fisher Scientific, Waltham, MA, Catalog number: 24040-032) for reducing non-specific cellular adhesion. The sample was then incubated with 125 ng $mL^{-1}$ of biotinylated anti-EpCAM monoclonal antibody (Biolegend, Inc., Clone: 9C4) on a rotator at 4 °C for 1 hour. After the first hour, streptavidin-functionalized magnetic nanoparticles (Ocean Nanotech, LLC, Catalog number: MHS-200-05) were added at a concentration of 10 μg $mL^{-1}$, and the mixture was further incubated on the rotator at 4 °C for another hour. After incubation, the samples were pumped through the sifter at a pre-set flow-rate in the presence of the permanent NdFeB magnet. An additional 1 mL of buffer was added after the sample had flowed through the device to wash the setup clean of residual blood before the NdFeB magnet was removed and the chip was imaged under the fluorescence microscope. Cell counts for the capture efficiency experiments were obtained manually.

Control experiments were run at both the highest and lowest flow rates for each set of sifters and holders, where cells were added without the addition of either the anti-EpCAM antibodies or the magnetic nanoparticles, or without the application of an external magnetic field during processing through the sifter. No cells were found on the sifter upon visual inspection with the microscope, hence verifying that there was no non-specific capture of the spiked cells for the cell concentrations tested.

### Experiments to Obtain Spatial Distribution of Captured Cells:

Spiked experiments were conducted as described above at flow rates of 10 mL $hr^{-1}$. This relatively slow flow rate was selected to ensure maximal capture efficiency on the sifter for observation of all capture locations. After the sample was passed through the sifter, microscope images of the sifter surface were acquired under both fluorescent and bright-

field mode. All fluid flow was done under continual application of the permanent NdFeB magnets. Acquired images were then loaded into ImageJ, where the fluorescent cells were identified and locations recorded relative to the center of the chip (identified manually from the bright-field image).[62] The cumulative probability distributions were then analyzed with the ks.test function from the R core software package.[63]

### Measurement of Driving Pressure across the Magnetic Sifter:

Sifters were assembled with custom laser-cut acrylic holders to permit water-tight connection with tubing on both the top and bottom of the sifter. A Dwyer Series 477 digital manometer (Michigan City, IN) was connected to the bottom tubing, and the gauge pressure was monitored when fluid was pumped through the sifter at flow rates between 10 - 40 mL $hr^{-1}$ via a syringe pump. Due to initial hysteresis in starting and the flow, the pressure measurements are only recorded upon the values reaching a stable equilibrium. Three runs were recorded for each flow rate, and averages and standard deviations were calculated accordingly.

### Comsol Multiphysics Numerical Simulations:

Finite-element numerical simulations of the fluid profile going through the magnetic sifter were done with a commercial simulation package (Comsol Multiphysics version 4.3). As the individual pores are not circular, and the honeycomb tessellation of individual hexagonal arrays is not circular, a 2-D axisymmetric assumption is not appropriate, and a sectorial cross-section is used for simulation instead. This reduced geometry capitalizes on the inherent symmetry of the magnetic sifter design, as the use of periodic boundary conditions allowed for a reduction in the total mesh size and hence, computational time, while still allowing for a fully explicit and accurate representation of the sifter geometry. The simulation geometry is extended in the z-direction to reflect the tubing that is used to feed the sample into the sifter, while a finer mesh is used in the vicinity of the sifter to accurately represent the individual micron-scale features. For the simulation, a series of volumetric flow rates spanning 10 – 40 mL $hr^{-1}$ across the magnetic sifter was used, and the Navier-Stokes equation was solved to obtain the fluidic flow profile. No magnetic forces or cells were included in the simulation as the flow profile is of primary concern. Additionally, at these flow rates, the Reynolds number of the flow is below 1, and turbulence effects are not included in the model. Standard properties for water were used for the fluid in the simulation, with a density of 1000 kg $m^{-3}$ and a viscosity of 0.001 cP.

## Acknowledgements

This work was supported by the Center for Cancer Nanotechnology Excellence (U54CA199075 and U54CA151459) and the Innovative Molecular Analysis Technologies (R33CA138330). The authors would also like to thank Dr. Andrew Wang, Ocean Nanotech, LLC for kindly providing the streptavidin-conjugated magnetic nanoparticles used in this work.

## References

[1]. Thorsen T, Maerkl SJ, and Quake SR, Science 2002, 298(5593), p. 580–584. [PubMed: 12351675]
[2]. Shapiro E, Biezuner T, and Linnarsson S, Nature Reviews Genetics 2013, 14(9), p. 618–630.
[3]. Kalisky T and Quake SR, Nature methods 2011, 8(4), p. 311–314. [PubMed: 21451520]

[4]. Elvira KS, Solvas X.C. i, and Wootton RC, Nature chemistry 2013, 5(11), p. 905–915.

[5]. Valencia PM, Farokhzad OC, Karnik R, and Langer R, Nature nanotechnology 2012, 7(10), p. 623–629.

[6]. Lenshof A and Laurell T, Chemical Society Reviews 2010, 39(3), p. 1203–1217. [PubMed: 20179832]

[7]. Inglis DW, Riehn R, Austin R, and Sturm J, Applied Physics Letters 2004, 85(21), p. 5093–5095.

[8]. Bhagat AAS, Bow H, Hou HW, Tan SJ, Han J, and Lim CT, Medical & biological engineering & computing 2010, 48(10), p. 999–1014. [PubMed: 20414811]

[9]. Gossett DR, Weaver WM, Mach AJ, Hur SC, Tse HTK, Lee W, Amini H, and Di Carlo D, Analytical and bioanalytical chemistry 2010, 397(8), p. 3249–3267. [PubMed: 20419490]

[10]. Pamme N, Lab on a Chip 2007, 7(12), p. 1644–1659. [PubMed: 18030382]

[11]. Yager P, Edwards T, Fu E, Helton K, Nelson K, Tam MR, and Weigl BH, Nature 2006, 442(7101), p. 412. [PubMed: 16871209]

[12]. Lee WG, Kim Y-G, Chung BG, Demirci U, and Khademhosseini A, Advanced drug delivery reviews 2010, 62(4-5), p. 449–457. [PubMed: 19954755]

[13]. Zborowski M and Chalmers JJ, Analytical Chemistry 2011, 83(21), p. 8050–8056. [PubMed: 21812408]

[14]. Cristofanilli M, Budd GT, Ellis MJ, Stopeck A, Matera J, Miller MC, Reuben JM, Doyle GV, Allard WJ, and Terstappen LW, N Engl J Med 2004, 2004(351), p. 781–791.

[15]. Hayes DF, Cristofanilli M, Budd GT, Ellis MJ, Stopeck A, Miller MC, Matera J, Allard WJ, Doyle GV, and Terstappen LW, Clinical Cancer Research 2006, 12(14), p. 4218–4224. [PubMed: 16857794]

[16]. Hou S, Chen J-F, Song M, Zhu Y, Jan YJ, Chen SH, Weng T-H, Ling D-A, Chen S-F, and Ro T, ACS nano 2017, 11(8), p. 8167–8177. [PubMed: 28721719]

[17]. Ozkumur E, Shah AM, Ciciliano JC, Emmink BL, Miyamoto DT, Brachtel E, Yu M, Chen P.-i., Morgan B, and Trautwein J, Science translational medicine 2013, 5(179), p. 179ra47–179ra47.

[18]. Sarioglu AF, Aceto N, Kojic N, Donaldson MC, Zeinali M, Hamza B, Engstrom A, Zhu H, Sundaresan TK, and Miyamoto DT, Nature methods 2015, 12(7), p. 685. [PubMed: 25984697]

[19]. Hou HW, Warkiani ME, Khoo BL, Li ZR, Soo RA, Tan DS-W, Lim W-T, Han J, Bhagat AAS, and Lim CT, Scientific reports 2013, 3, p. 1259. [PubMed: 23405273]

[20]. Warkiani ME, Guan G, Luan KB, Lee WC, Bhagat AAS, Chaudhuri PK, Tan DS-W, Lim WT, Lee SC, and Chen PC, Lab on a Chip 2014, 14(1), p. 128–137. [PubMed: 23949794]

[21]. Dong Y, Skelley AM, Merdek KD, Sprott KM, Jiang C, Pierceall WE, Lin J, Stocum M, Carney WP, and Smirnov DA, The Journal of Molecular Diagnostics 2013, 15(2), p. 149–157. [PubMed: 23266318]

[22]. Jan YJ, Chen J-F, Zhu Y, Lu Y-T, Chen SH, Chung H, Smalley M, Huang Y-W, Dong J, and Chen L-C, Advanced drug delivery reviews 2018.

[23]. Warkiani ME, Tay AKP, Guan G, and Han J, Scientific reports 2015, 5, p. 11018. [PubMed: 26154774]

[24]. Hansson J, Karlsson JM, Haraldsson T, Brismar H, van der Wijngaart W, and Russom A, Lab on a Chip 2012, 12(22), p. 4644–4650. [PubMed: 22930164]

[25]. Miltenyi S, Müller W, Weichel W, and Radbruch A, Cytometry 1990, 11(2), p. 231–238. [PubMed: 1690625]

[26]. Zborowski M, Sun L, Moore LR, Williams PS, and Chalmers JJ, Journal of Magnetism and Magnetic Materials 1999, 194(1), p. 224–230.

[27]. Zheng S, Lin HK, Lu B, Williams A, Datar R, Cote RJ, and Tai Y-C, Biomedical microdevices 2011, 13(1), p. 203–213. [PubMed: 20978853]

[28]. Chalmers JJ, Zborowski M, Sun L, and Moore L, Biotechnology progress 1998, 14(1), p. 141–148. [PubMed: 9496679]

[29]. Yang L, Lang JC, Balasubramanian P, Jatana KR, Schuller D, Agrawal A, Zborowski M, and Chalmers JJ, Biotechnology and bioengineering 2009, 102(2), p. 521–534. [PubMed: 18726961]

[30]. Earhart CM, Hughes CE, Gaster RS, Ooi CC, Wilson RJ, Zhou LY, Humke EW, Xu L, Wong DJ, Willingham SB, Schwartz EJ, Weissman IL, Jeffrey SS, Neal JW, Rohatgi R, Wakelee HA, and Wang SX, Lab Chip 2014, 14(1), p. 78–88. [PubMed: 23969419]

[31]. Laws E and Livesey J, Annual Review of Fluid Mechanics 1978, 10(1), p. 247–266.

[32]. Loehrke R and Nagib H, Journal of Fluids Engineering 1976, 98(3), p. 342–351.

[33]. Mehta RD and Bradshaw P, The Aeronautical Journal 1979, 83(827), p. 443–453.

[34]. Scheiman J and Brooks J, Journal of Aircraft 1981, 18(8), p. 638–643.

[35]. Lee G-B, Lin C-H, and Chang S-C, Journal of Micromechanics and Microengineering 2004, 15(3), p. 447.

[36]. Goda K, Ayazi A, Gossett DR, Sadasivam J, Lonappan CK, Sollier E, Fard AM, Hur SC, Adam J, and Murray C, Proceedings of the National Academy of Sciences 2012, 109(29), p. 11630–11635.

[37]. Zhe J, Jagtiani A, Dutta P, Hu J, and Carletta J, Journal of Micromechanics and Microengineering 2007, 17(2), p. 304.

[38]. Kummrow A, Theisen J, Frankowski M, Tuchscheerer A, Yildirim H, Brattke K, Schmidt M, and Neukammer J, Lab on a Chip 2009, 9(7), p. 972–981. [PubMed: 19294310]

[39]. Oakey J, Applegate RW, Arellano E, Carlo DD, Graves SW, and Toner M, Analytical Chemistry 2010, 82(9), p. 3862–3867. [PubMed: 20373755]

[40]. Bhargava KC, Thompson B, and Malmstadt N, Proceedings of the National Academy of Sciences 2014, 111(42), p. 15013–15018.

[41]. Park S.-m., Wong DJ, Ooi CC, Kurtz DM, Vermesh O, Aalipour A, Suh S, Pian KL, Chabon JJ, Lee SH, Jamali M, Say C, Carter JN, Lee LP, Kuschner WG, Schwartz EJ, Shrager JB, Neal JW, Wakelee HA, Diehn M, Nair VS, Wang SX, and Gambhir SS, Proceedings of the National Academy of Sciences 2016, 113(52), p. E8379–E8386.

[42]. Ooi C, Earhart CM, Wilson RJ, and Wang SX, IEEE transactions on magnetics 2013, 49(1), p. 316–320. [PubMed: 23515873]

[43]. Davami K, Zhao L, and Bargatin I, IEEE 27th International Conference on Micro Electro Mechanical Systems (MEMS) 2014, p.449–452.

[44]. Massey FJ Jr, Journal of the American statistical Association 1951, 46(253), p. 68–78.

[45]. Young IT, Journal of Histochemistry & Cytochemistry 1977, 25(7), p. 935–941. [PubMed: 894009]

[46]. Dagan Z, Weinbaum S, and Pfeffer R, Journal of Fluid Mechanics 1982, 115, p. 505–523.

[47]. Muluneh M, Shang W, and Issadore D, Advanced Healthcare Materials 2014, 37, p. 1078–1085. [PubMed: 24535921]

[48]. Ko J, Bhagwat N, Yee SS, Black T, Redlinger C, Romeo J, O'Hara M, Raj A, Carpenter EL, Stanger BZ, and Issadore D, Lab on a Chip 2017, 17(18), p.3086–3096. [PubMed: 28809985]

[49]. Ravnkilde JT, Ziebart V, Hansen O, and Baltes H, Sensors and Materials 2000, 12(2), p. 99–108.

[50]. Li X, Ding G, Wang H, Ando T, Shikida M, and Sato K, International Conference on Solid State Sensors and Actuators (TRANSDUCERS) 2007, p. 555–558.

[51]. Wygant IO, Kupnik M, and Khuri-Yakub BT, IEEE Ultrasonics Symposium 2008, p. 2111–2114.

[52]. Timoshenko S, and Woinowsky-Krieger S, Theory of Plates and Shells. 1959, McGraw-Hill.

[53]. Zhao H, Shaqfeh ESG, and Narsimhan V, Physics of Fluids 2012, 24(1): 011902.

[54]. Zhao H and Shaqfeh ESG, Physical Review E 2011, p. 061924.

[55]. Poudineh M, Sargent EH, and Kelley SO, ACS Applied Materials & Interfaces 2017, 9(31), p. 25683–25690. [PubMed: 28696666]

[56]. Poudineh M, Aldridge PM, Ahmed S, Green BJ, Kermanshah L, Nguyen V, Tu C, Mohamadi RM, Nam RK, Hansen A, Sridhar SS, Finelli A, Fleshner NE, Joshua AM, Sargent EH, and Kelley SO, Nature Nanotechnology 2016, 12, p. 274.

[57]. Kwak B, Lee J, Lee D, Lee K, Kwon O, Kang S, and Kim Y, Biosensors and Bioelectronics 2017, 88(Supplement C), p. 153–158. [PubMed: 27503409]

[58]. Mohamadi RM, Besant JD, Mepham A, Green B, Mahmoudian L, Gibbs T, Ivanov I, Malvea A, Stojcic J, and Allan AL, Angewandte Chemie International Edition 2015, 54(1), p. 139–143. [PubMed: 25377874]

[59]. Pamme N, Koyama R, and Manz A, Lab on a Chip 2003, 3(3), p. 187–192. [PubMed: 15100772]

[60]. Bailey RC, Kwong GA, Radu CG, Witte ON, and Heath JR, Journal of the American Chemical Society 2007, 129(7), p. 1959–1967. [PubMed: 17260987]

[61]. Waters LC, Jacobson SC, Kroutchinina N, Khandurina J, Foote RS, and Ramsey JM, Analytical chemistry 1998, 70(1), p. 158–162. [PubMed: 9463271]

[62]. Schneider CA, Rasband WS, and Eliceiri KW, Nature methods 2012, 9(7), p. 671–675. [PubMed: 22930834]

[63]. R.D.C. Team, R: A Language and Environment for Statistical Computing. 2008, R Foundation for Statistical Computing.

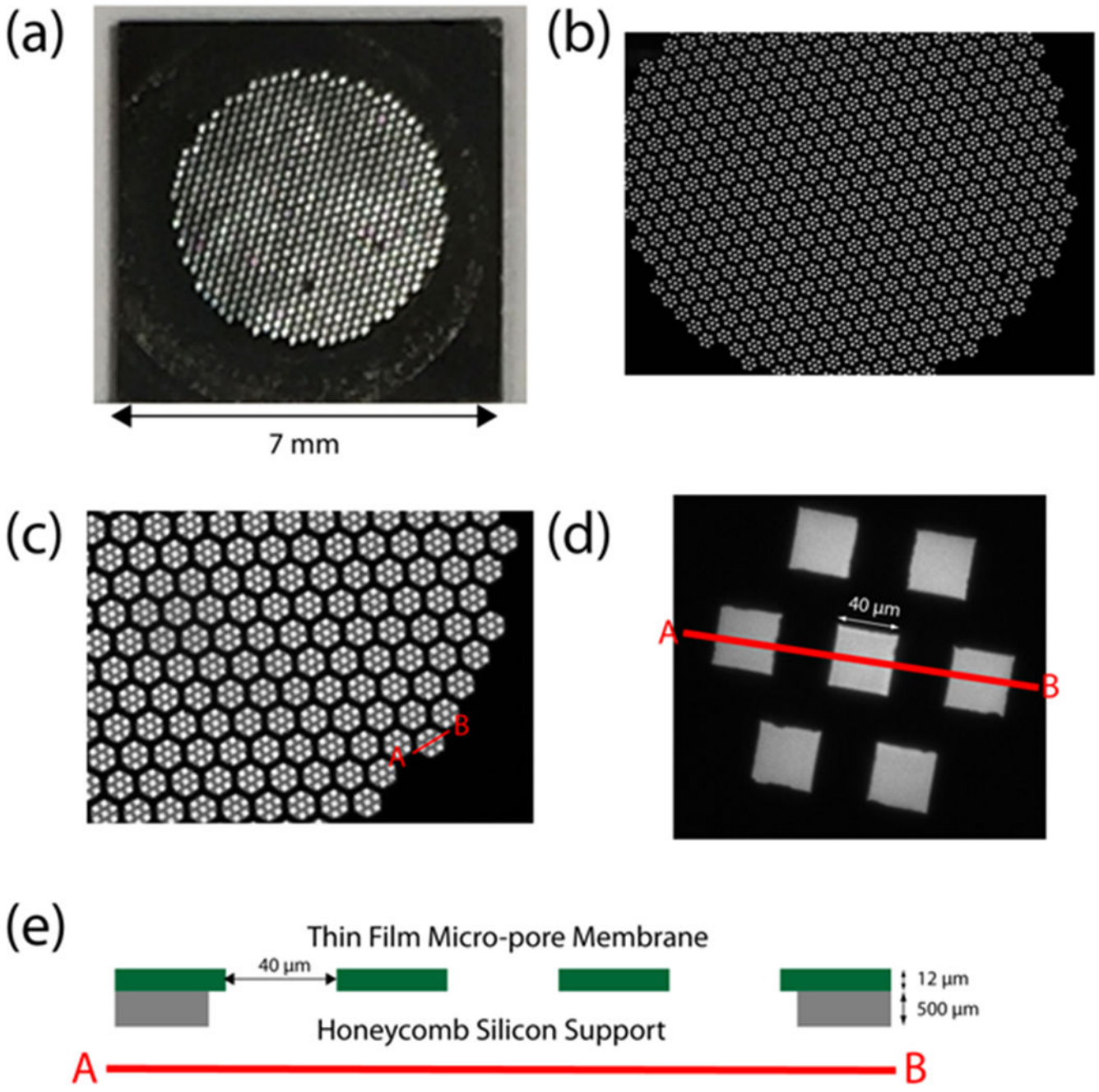


**Figure 1.**

(a) Photograph of the magnetic sifter. The device is a 7 × 7 $mm^2$ silicon chip, and the micro-pores are distributed uniformly within a 5-mm diameter circular region in the chip's center. (b) A bright-field microscope image of the micro-pores that make up the device. (c) A magnified bright-field microscope image of part of the sifter. The honeycomb silicon skeleton appears black as it is solid and blocks light transmission. The thin metal film appears gray as it only partially blocks transmission of light due to its thickness, and is evident between the 7 individual pores (white) in each group. (d) A bright-field microscope image of a group of 7 micro-pores in the array. (e) Schematic of the side profile of the sifter,

illustrating how the 40 × 40 $\mu m^2$ micro-pores in a thin film membrane are supported on the 7 × 7 $mm^2$ silicon chip. The red lines (A-B) indicate correspondence between the side view in (e) and top-down images in (c) and (d).

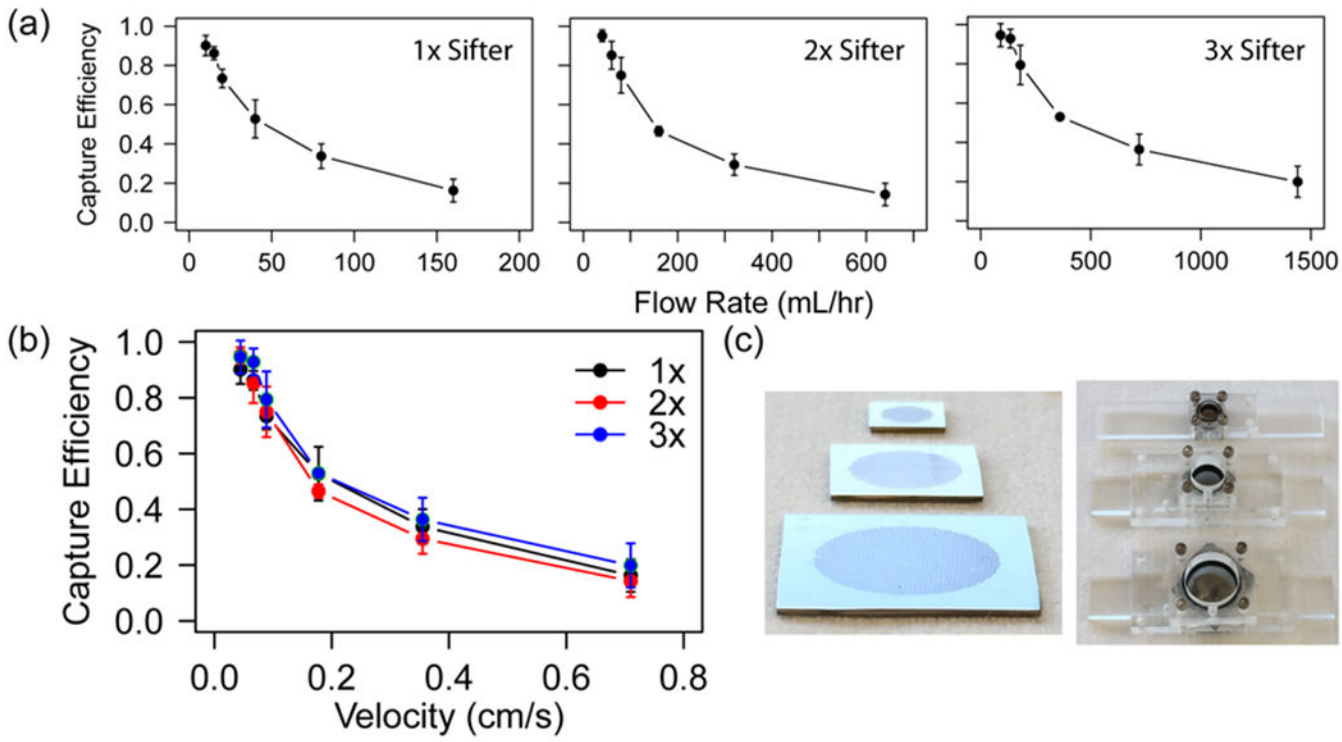


**Figure 2.**

(a) Capture efficiencies of the magnetic sifter across sifters of 3 different sizes, with 1X sifters having 5 × 5 $mm^2$ active area, 2X sifters having 10 × 10 $mm^2$ active area, and 3X sifters having 15 × 15 $mm^2$ active area. (b) Capture efficiencies are replotted against average linear velocity of fluid through each sifter, as calculated by the volumetric flow rate and the total surface area of all pores in each chip. A good overlap is observed in their capture performance regardless of chip size. (c) Pictures of the 1X, 2X and 3X chips are presented, along with their corresponding acrylic custom-made holders.

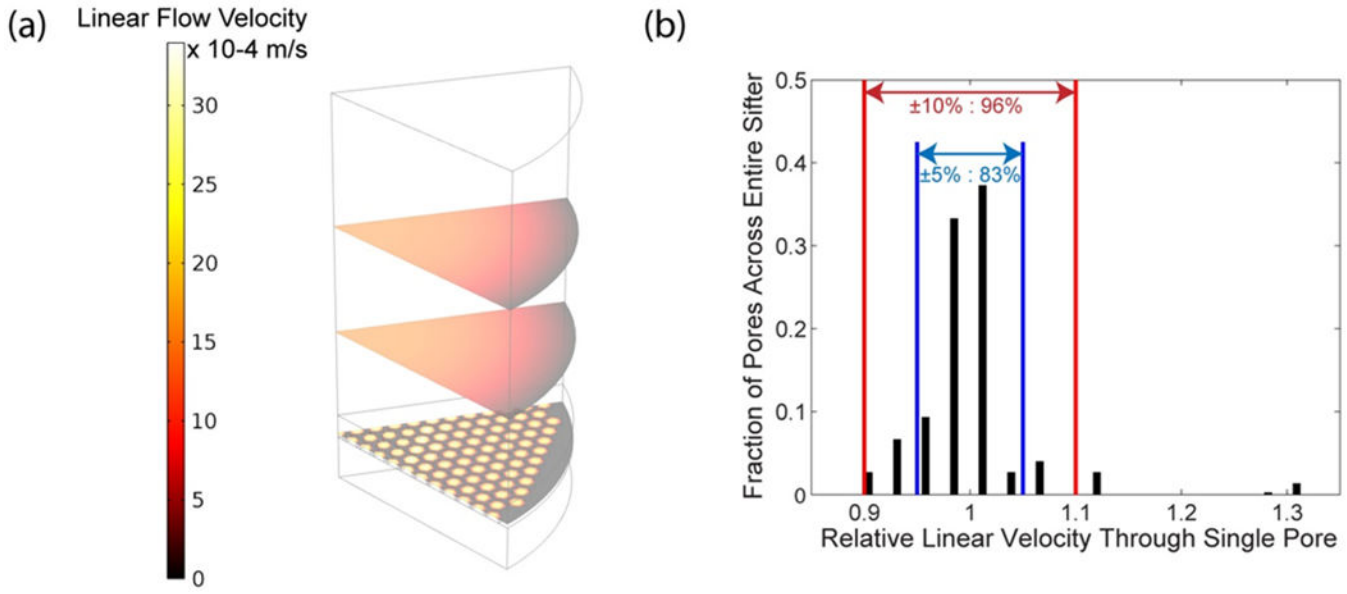


**Figure 3.**

(a) Comsol Multiphysics simulations reveal how the initially parabolic velocity profile within the sifter gradually transitions to consistent flow velocities across each individual pore within the sifter at distances nearer to the sifter. Slices depict linear flow velocity at 3 locations upstream of the sifter (3 mm, 1.5 mm, and 0.1 mm above the sifter surface). (b) An analysis of the average linear velocity in each individual pore for all sifter pores show that 96 % of the pores have flow velocities within 10 % of each other. The linear velocities have been normalized to the average velocity across all pores in a single sifter.

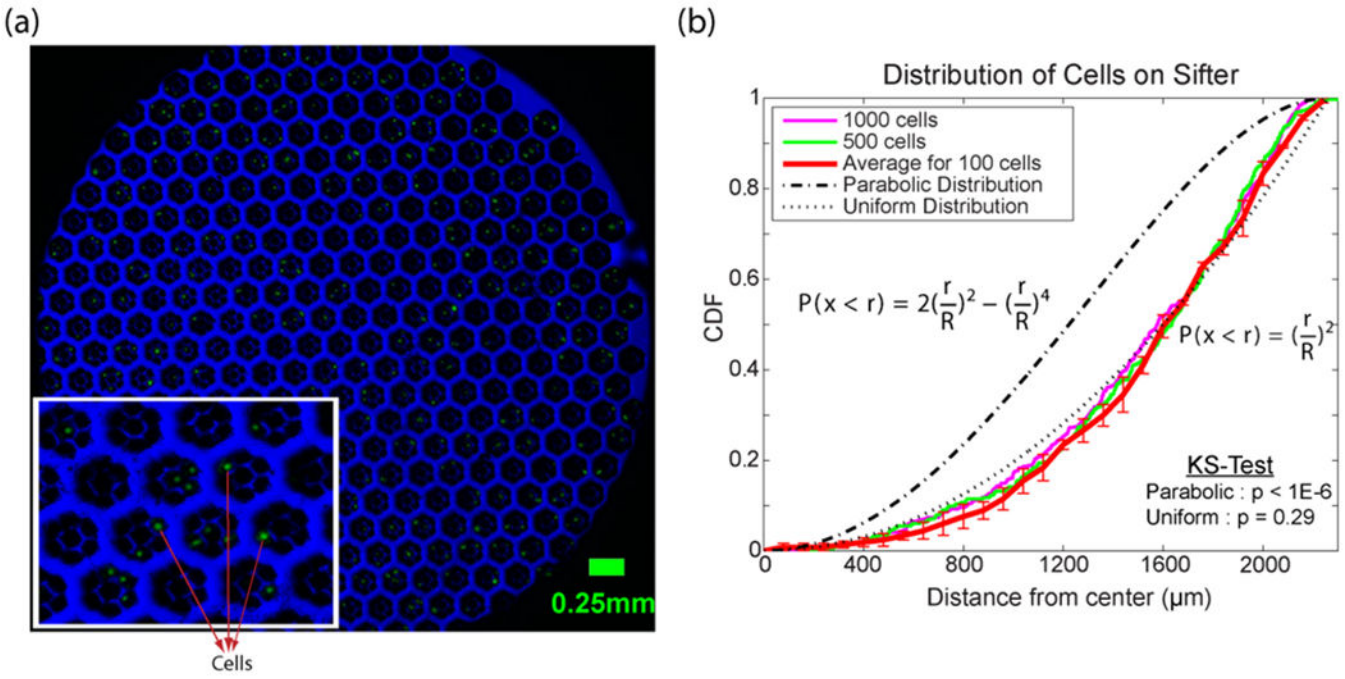


**Figure 4.**

(a) An example of a merged fluorescent microscopy image of the sifter after passage and capture of the magnetically labeled H1650 cells. The H1650 cells have been stained with a green fluorescent dye for facile detection and image analysis. A bright-field image (blue) is used for identification of the center of the chip for determining the cells' spatial location. Inset shows examples of the green cells that have been captured on the sifter. (b) The spatial distribution of the captured cells on the sifter is plotted as a cumulative distribution function (CDF) in terms of the cells' distance from the center of the sifter. Two expected distributions are also plotted, corresponding to the spatial distribution expected with either a parabolic (laminar) or uniform flow. A set of 5 runs with 100 cells per run, and 2 runs with 500 and 1000 cells per run are also plotted, to illustrate the lack of saturation effects.

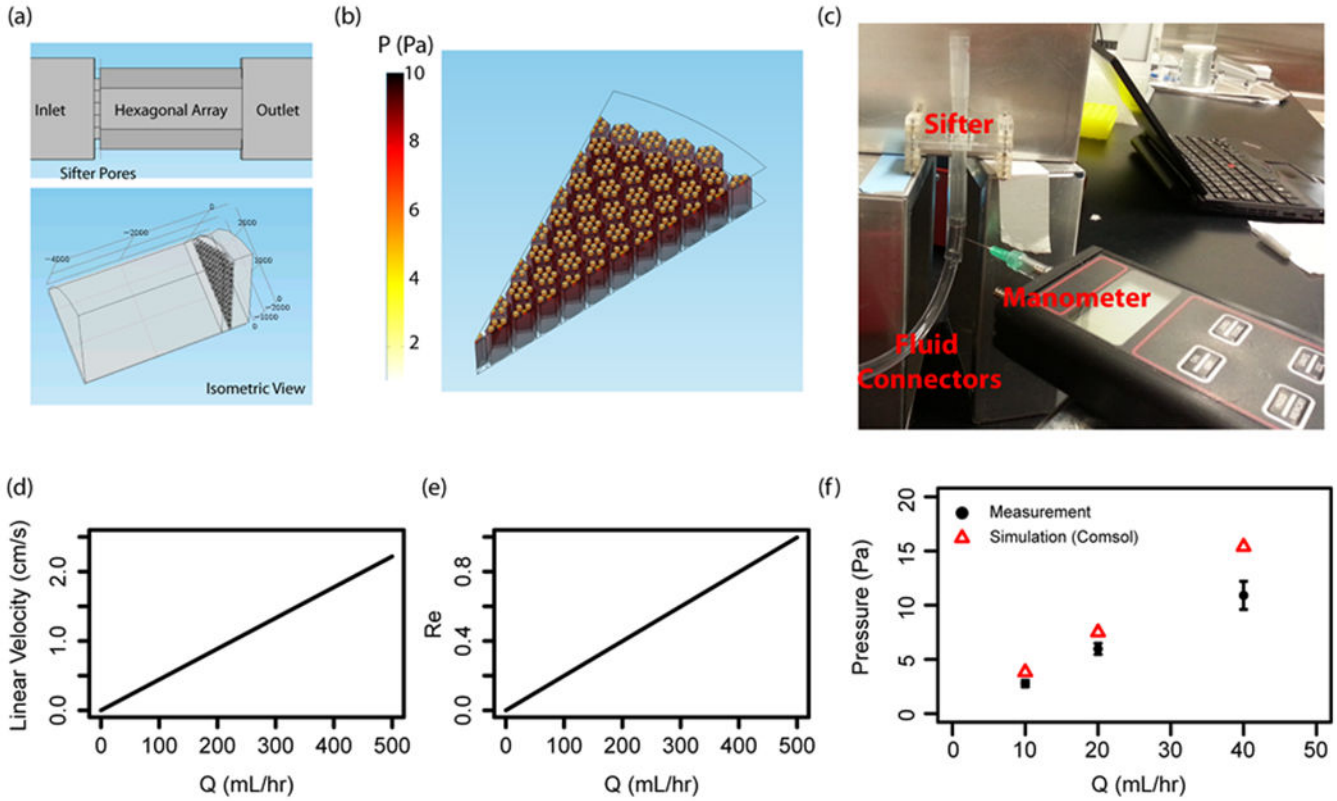


**Figure 5.**

(a) and (b) are images of the simulated geometry from Comsol Multiphysics, along with the pressure distribution through the individual pores of the sifter. (c) is an illustration of the experimental setup used for measuring the driving pressure required to pump fluid through the sifter at a particular flow rate. (d) and (e) are plots of the relative linear velocity through a sifter with a $5 \times 5$ mm$^2$ active area (1X sifter), and the associated Reynolds number at various volumetric flow rates, showing how the flow remains largely within the laminar regime at high volumetric flow rates. (f) is a plot of the pressure difference across the magnetic sifter from experimental measurements and Comsol Multiphysics numerical simulations.

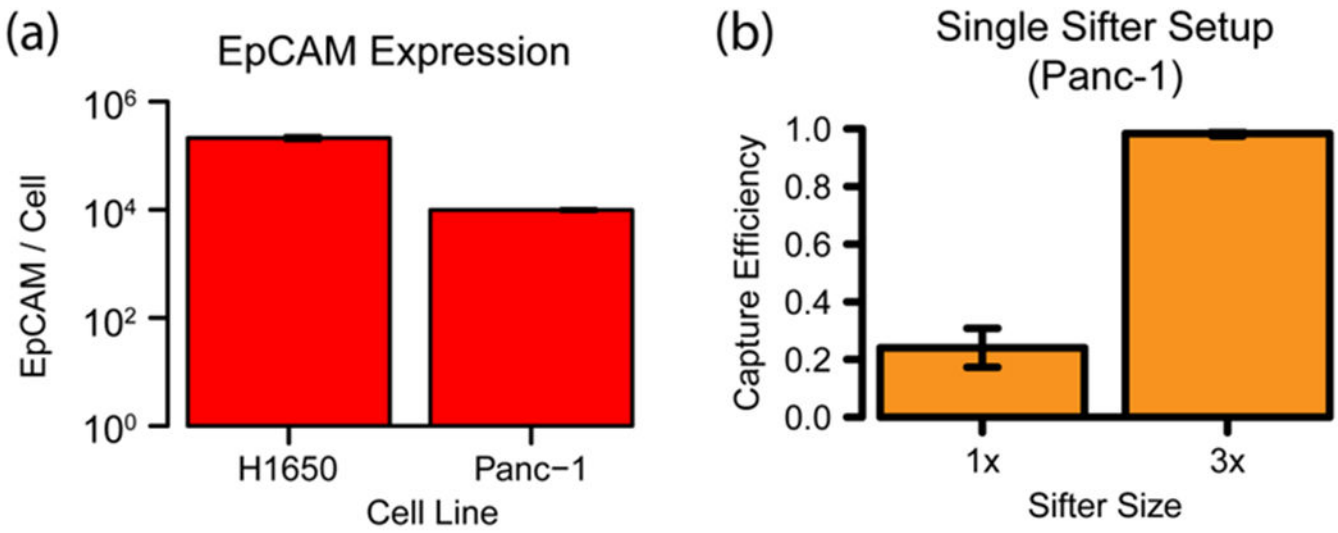


**Figure 6.**

(a) EpCAM expression levels for the H1650 and Panc-1 cell lines as measured by flow cytometry. (b) Capture efficiencies for Panc-1 when processed with the 1X and the 3X sifters at a flow rate of 10 mL $hr^{-1}$.

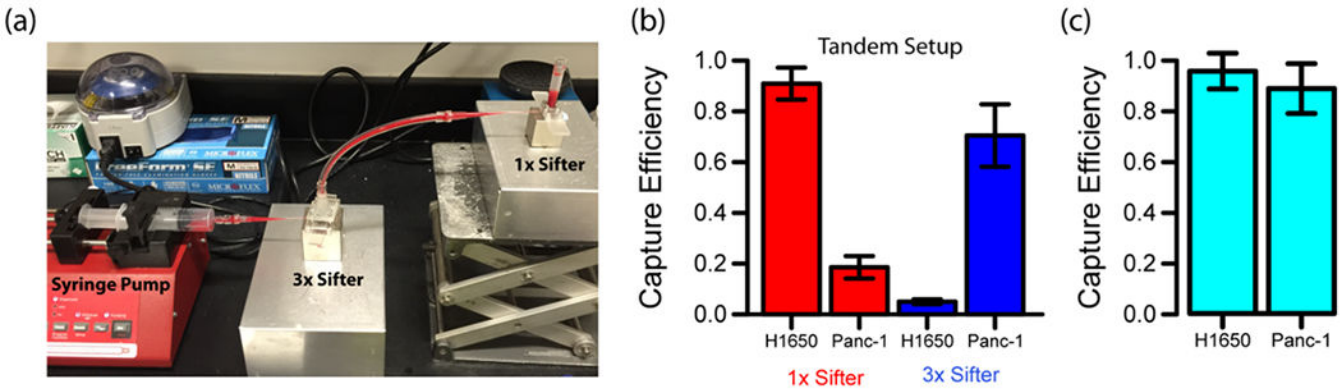


**Figure 7.**

(a) Image of the tandem setup incorporating 2 differently-sized sifters in the processing of a single sample at a unified volumetric flow rate. (b) Capture efficiencies for a heterogeneous mix of H1650 and Panc-1 cells processed with the tandem setup portrayed in (a). The H1650 cells are primarily captured on the 1X sifter (83% purity), while the Panc-1 cells are primarily captured on the 3X sifter (93% purity). (c) The combined capture efficiency for both cell lines remains high in the tandem system, with 93% of H1650 cells and 89% of Panc-1 cells still successfully captured across the two chips in the tandem system, which is consistent with previously reported capture efficiencies on the single sifter systems.